Research Article

ADVANCED PHOTONICS

Spatiotemporal-multiplexed Fourier ptychographic diffraction tomography for high-speed, label-free 3D imaging of live cells

Shun Zhou,[a,b,c] Qian Shen,[a,b,c] Habib Ullah,[a,b,c] Kaiyu Du,[a,b,c] Linpeng Lu,[a,b,c] Hongjun Wu,[a,b,c] Yao Fan,[a,b,c] Jiasong Sun,[a,b,c,d] Dayong Jin,[e,*] Qian Chen,[c,d,*] and Chao Zuo[a,b,c,d,*]

[a]Nanjing University of Science and Technology, School of Electronic and Optical Engineering, Smart Computational Imaging Laboratory (SCILab), Nanjing, China
[b]Smart Computational Imaging Research Institute (SCIRI) of Nanjing University of Science and Technology, Nanjing, China
[c]Jiangsu Key Laboratory of Visual Sensing & Intelligent Perception, Nanjing, China
[d]State Key Laboratory of Extreme Environment Optoelectronic Dynamic Measurement Technology and Instrument, Taiyuan, China
[e]University of Technology Sydney, Institute for Biomedical Materials and Devices (IBMD), Faculty of Science, Sydney, New South Wales, Australia

Abstract. Label-free, three-dimensional (3D) imaging of organelle dynamics at high spatiotemporal resolution is essential for deciphering cellular physiology. While optical diffraction tomography (ODT) can retrieve intrinsic-contrast 3D refractive-index distribution of transparent cells, its sequential, variable-angle acquisition compromises temporal resolution, obscuring rapid events such as membrane blebbing, vesicle trafficking, and cytoskeletal remodeling. Here, we introduce spatiotemporal-multiplexed Fourier ptychographic diffraction tomography (STM-FPDT), a noninterferometric ODT modality that employs hybrid coherent/partially coherent annular illumination to achieve high resolution in both space ($x-y-z$) and time (t). By integrating a spatiotemporal reconstruction framework with a sliding window protocol and nonlinear global optimization, STM-FPDT achieves volumetric imaging at 5 Hz with 347 nm lateral and 1.54 μm axial resolution over a 40×/0.75 NA objective. We validate STM-FPDT across diverse cell lines, successfully capturing membrane blebbing, mitochondrial fission, and intercellular interactions that evade conventional ODT. Readily retrofittable to standard bright-field microscopes, STM-FPDT offers a broadly accessible platform for quantitative, high-spatiotemporal-resolution studies of live-cell physiology.

Keywords: diffraction tomography; live-cell imaging; refractive index imaging; 3D microscopy.

Received Nov. 3, 2025; revised manuscript received Dec. 30, 2025; accepted for publication Jan. 16, 2026; published online Feb. 15, 2026.

[DOI: 10.1117/1.AP.8.2.026003]

1 Introduction

As Leeuwenhoek's simple single-lens device first revealed the microbial world four centuries ago,[1,2] optical microscopy has evolved into a sophisticated metrological instrument capable of resolving micro-scale structures with high resolution, spanning from nanometer-scale molecular machinery to micrometer-scale cellular architectures.[3,4] This progress has been propelled by two key performance pillars—resolution and contrast—particularly in biological imaging, where cells and tissues are naturally transparent and exhibit low-contrast features.[5] Recent breakthroughs in super-resolution fluorescence microscopy now routinely deliver nanometer spatial resolution with exceptional molecular specificity.[6–12] However, fluorescent labeling is not suitable for organelles or components that cannot be easily tagged, such as certain native proteins and extracellular matrix elements.[13,14] Moreover, exogenous contrast agents can perturb cellular physiology, affecting cell viability, proliferation, and differentiation. Photobleaching and phototoxicity further constraints on longitudinal live-cell imaging, hindering investigations requiring sustained observation.[15,16]

*Address all correspondence to Chao Zuo, zuochao@njust.edu.cn; Qian Chen, chenqian@njust.edu.cn; Dayong Jin, dayong.jin@uts.edu.au

Phase imaging offers a label-free alternative for high-contrast biological cell imaging by exploiting intrinsic refractive index (RI) variations as an endogenous contrast mechanism. Pioneered by Zernike's 1930s phase contrast microscopy, which converted phase differences into amplitude variations via wavefront filtering and later earned a Nobel Prize,[17] phase imaging evolved with interferometric digital holography to achieve quantitative phase measurement.[18–20] Notably, optical diffraction tomography (ODT) introduced by Wolf in 1969 marked a paradigm shift in phase imaging, enabling 3D visualization akin to confocal microscopy through holography-tomography fusion to infer volumetric RI distributions.[21–26] Yet conventional ODT implementations face some bottlenecks: their reliance on vibration-sensitive laser interferometry induces speckle artifacts and leads to a degradation in spatial resolution. Although recently some noninterferometric ODT methods based on LED illumination have been proposed to simplify the system configurations and enhance imaging quality,[27–32] a fundamental speed bottleneck persists due to the requirement for sequential variable-angle illumination to achieve sufficient Fourier space coverage. Although illumination multiplexing schemes[33,34] and partially coherent strategies[33,35] have been actively explored to increase acquisition rates, most of these approaches remain confined to two-dimensional phase imaging. Extending ODT to partially coherent illumination typically necessitates mechanical axial scanning to acquire defocused intensity stacks, which imposes an intrinsic limitation on temporal resolution.[36–38] Furthermore, ODT employing sparse sampling improves imaging speed by reducing the number of acquired measurements, albeit often at the expense of reconstruction quality.[39,40] Collectively, these constraints severely impede the application of ODT to subcellular dynamics occurring on millisecond timescales, thereby creating a critical mismatch between current technical capabilities and the growing demands of longitudinal live-cell imaging.

Here, we report on a motion-free noninterferometric ODT technique tailored for live-cell dynamic 3D imaging, termed spatiotemporal-multiplexed Fourier ptychographic diffraction tomography (STM-FPDT). STM-FPDT innovatively extends traditional FPDT's spatial coherent imaging mechanism to coherent/partially coherent (C/PC) hybrid imaging mechanism. By employing an objective numerical aperture (NA)-matched annular C/PC hybrid illumination strategy, this method effectively retains phase contrast while enabling parallel spectral acquisition.[35,41] To solve the inverse reconstruction problem, we further develop a spatiotemporal collaborative tomographic reconstruction framework integrating the sliding window protocol and the nonlinear global optimization.[42] Capitalizing on biological structures' spatiotemporal continuity priors across $x-y-z-t$ domains as physical constraints,[43] STM-FPDT enables volumetric RI reconstruction from only 11 intensity images, achieving 3D tomography at 5 Hz volumetric rates with 347 nm lateral/1.54 μm axial resolution while eliminating motion artifacts associated with subcellular dynamic events. Validated through longitudinal monitoring of primary liver cancer (PLC) cells, STM-FPDT reveals previously inaccessible sub-second organelle dynamics, including membrane blebbing, cytoskeletal fiber fluctuations, and mitochondrial fission during metabolic adaptation. Crucially, STM-FPDT requires minimal bright-field microscope modifications, enabling a cost-effective transformation of standard microscopes into reliable 3D computational imagers. This platform establishes a new paradigm for label-free investigation of subcellular physiological processes at native spatiotemporal scales, with particular utility for studying rapid organelle interactions in vulnerable primary cell cultures.

2 Results

2.1 Principle of STM-FPDT

When an object is illuminated by a plane wave, light–matter interaction causes significant perturbations in the resulting transmitted field due to the spatially varying RI distribution [Fig. 1(a)]. The transmitted field contains the incident field and scattered field (see Sec. 4). Fourier ptychographic diffraction tomography (FPDT),[27,39] as a noninterferometric ODT technique, reconstructs the 3D RI distribution using only intensity measurements of the scattered field, enabling deployment on standard bright-field microscopes. Figure 1(b) illustrates the simplified optical configuration where both incident illumination (green) and scattered light (red) share identical optical paths to the detector, eliminating the need for an interference configuration. However, conventional FPDT relies on coherent detection, requiring sequential acquisition of scattered fields under variable-angle plane wave illumination to achieve adequate spectrum sampling, so as to alleviate the ill-posedness of the inverse scattering solution. This serial acquisition severely limits temporal resolution, precluding the capture of rapid cellular dynamics.

The developed STM-FPDT extends conventional coherent diffraction tomography to a hybrid C/PC imaging framework. Under coherent plane wave illumination $U_{\text{in}}(\mathbf{r})$, the relationship between the object function $O(\mathbf{r})$ and the first-order scattered field $U_{s1}(\mathbf{r})$ follows the Fourier diffraction theorem[21] (see Sec. 4):

$$\hat{O}(\mathbf{u}-\mathbf{u}_{\text{in}}) = 4\pi j u_z \hat{U}_{s1}(\mathbf{u}_T) P_{3\text{D}}(\mathbf{u}), \tag{1}$$

where $\mathbf{u} = (\mathbf{u}_T, u_z) = (u_x, u_y, u_z)$ represents the 3D spatial frequency coordinates corresponding to 3D spatial coordinate $\mathbf{r} = (\mathbf{r}_T, z) = (x, y, z)$, and $\mathbf{u}_{\text{in}}$ is the 3D incident plane wave vector. $\hat{O}$ and $\hat{U}_{s1}$ correspond to the 3D and 2D Fourier transforms of $O(\mathbf{r})$ and $U_{s1}(\mathbf{r}_T)$, respectively. $P_{3\text{D}}(\mathbf{u})$ is defined as the 3D coherent transfer function. The forward intensity-formation model for STM-FPDT in C/PC imaging under the Rytov approximation is given by

$$\begin{cases} I_c(\mathbf{r}_T) = \left| U_{\text{in}}(\mathbf{r}_T, \mathbf{u}_{\text{in}}) \exp\left[\frac{U_{s1}(\mathbf{r}_T)}{U_{\text{in}}(\mathbf{r}_T, \mathbf{u}_{\text{in}})}\right] \right|^2, & \text{coherent field} \\ I_{\text{pc}}(\mathbf{r}_T) = \sum_{l=1}^{L} \left| U_{\text{in},l}(\mathbf{r}_T, \mathbf{u}_{\text{in},l}) \exp\left[\frac{U_{s1,l}(\mathbf{r}_T)}{U_{\text{in},l}(\mathbf{r}_T, \mathbf{u}_{\text{in},l})}\right] \right|^2, & \text{partially coherent field} \end{cases}, \tag{2}$$

where L is the number of discrete plane waves under partially coherent illumination. As plane waves from different illumination angles do not satisfy the conditions for coherent interference, the resulting intensity under partially coherent illumination follows the principle of incoherent superposition, corresponding to the sum of the intensities contributed by

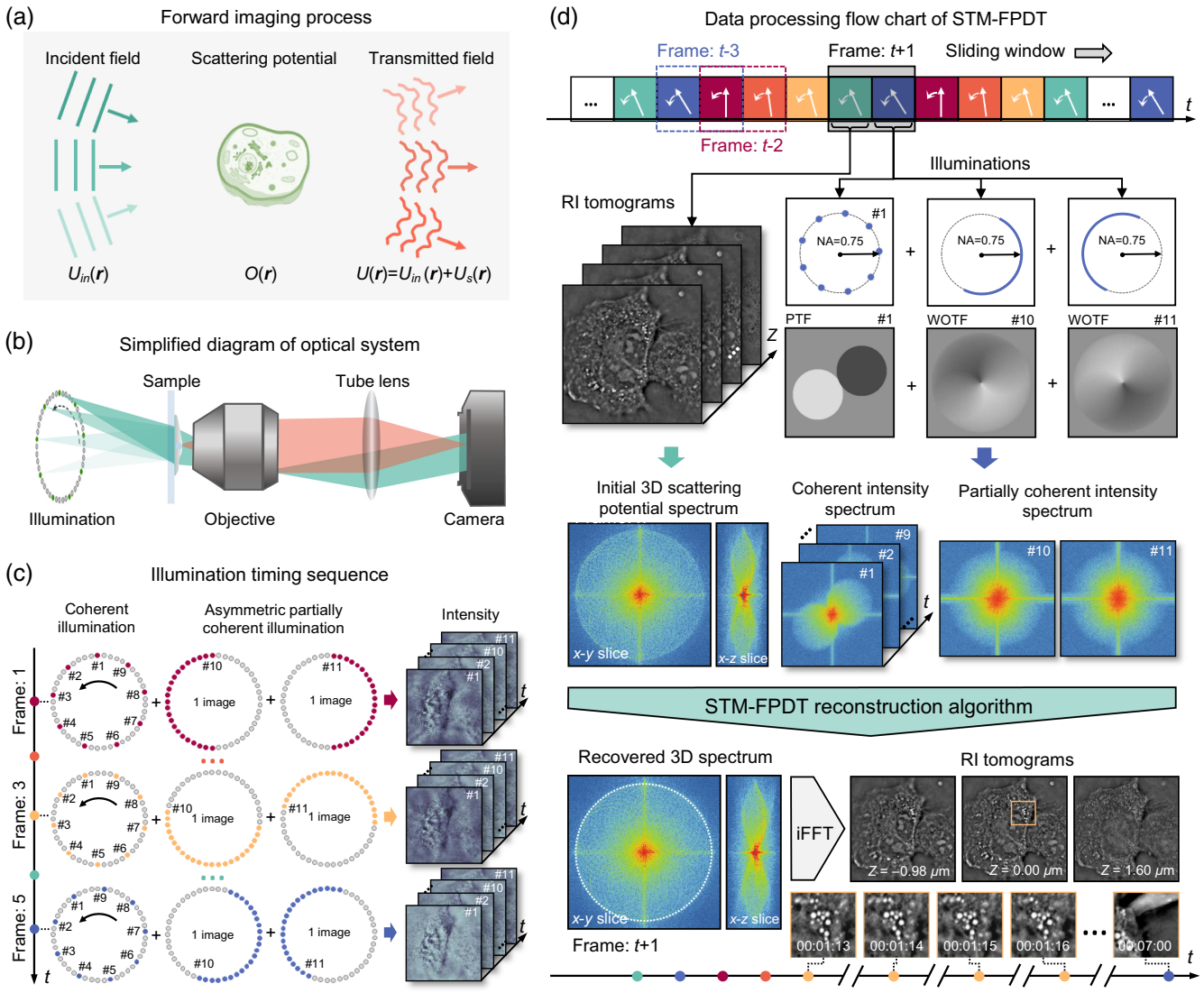

Fig. 1 Schematic of the STM-FPDT system for label-free 3D imaging of live cells. (a) Object $O(\mathbf{r})$ is illuminated by the variable-angle plane wave $U_{\text{in}}(\mathbf{r})$, and the total transmitted field $U(\mathbf{r})$ generated includes the incident field $U_{\text{in}}(\mathbf{r})$ and the scattered field $U_s(\mathbf{r})$. (b) Simplified diagram of the illumination and imaging system of the non-interferometric ODT platform. (c) By synchronizing the camera and LED trigger, the LED elements are illuminated according to the designed timing sequence, and the intensity of the forward field is recorded, where each frame contains 11 raw intensity images. (d) Data processing flow chart of STM-FPDT for 3D RI reconstruction using unstained PLC cells as an example. PTF, phase transfer function; WOTF, weak object transfer function.

each plane wave (see Note 2 in the Supplementary Material). This enables spatial information multiplexing, allowing parallel acquisition of scattering potential information within a single measurement and thereby enhancing data acquisition efficiency.

We implemented STM-FPDT on a commercial microscope with a programmable annular LED array comprising 45 individually addressable elements as the illumination source (see Sec. 4 and Fig. S2 in the Supplementary Material for detailed hardware specifications). Numerical validation confirmed the array's capability for sufficient spectral sampling (see Note 1 and Fig. S1 in the Supplementary Material). Figure 1(c) visually depicts the precise arrangement of illumination per frame, demonstrating a cyclical configuration (see Sec. 4 and Table S1 in the Supplementary Material for a detailed description). This designed illumination strategy enhances both data acquisition efficiency and reconstruction robustness through complementary phase transfer function (PTF)/weak object transfer function (WOTF) modulation and spectral diversity.[41,44] It features four key concepts. First, NA-matched annular illuminations balance robust low-frequency phase response with incoherent diffraction-limited resolution.[41,45] Second, two asymmetric semi-annular illuminations enable parallel acquisition of scattering potential spectrum while maintaining phase contrast, substantially

improving data acquisition efficiency.[35] Meanwhile, nine coherent components ensure that distinct portions of the scattered field are recorded independently, providing data redundancy essential for stable iterative reconstruction while minimizing data accumulation (see Note 1 and Fig. S3 in the Supplementary Material). Finally, the revolving illumination strategy enables independent acquisition of scattering fields under each illumination angle over extended periods, thereby alleviating the burden of field de-multiplexing during reconstruction and ensuring stable, long-term imaging performance.

For RI reconstruction, we developed a spatiotemporal collaborative tomographic reconstruction framework to solve the inverse scattering problem. Specifically, the reconstruction process of STM-FPDT is formulated as an optimization problem that seeks to estimate the scattering potential (or RI) by minimizing the cost function

$$\min_{O} \frac{1}{2K} \sum_{k=1}^{K} \|S_k(O) - I_k^m\|_{\ell_2}^2 + \tau_{xyz} \|D_{xyz}(O)\|_{\ell_2} + \tau_t \|D_t(O)\|_{\ell 2}. \tag{3}$$

The first term describes how well the current estimated intensities fit the actual measurements I_k^m, where $S_k(\cdot)$ is the forward operator computed via Eqs. (1) and (2). K is the number of measurement intensity images. Based on Fourier diffraction theorem, STM-FPDT adopts an intensity-constrained iterative optimization algorithm that integrates the strategy of difference map[42] to update the scattering potential spectrum. The update equation is expressed as

$$\hat{O}^{\text{new}}(\mathbf{u}) = \hat{O}(\mathbf{u}) + \alpha \left[\frac{\sum_{i=1}^{N} P_{3D}^{*}(\mathbf{u} + \mathbf{u}_{\text{in},i}) \hat{O}_i^{\text{new}}(\mathbf{u})}{\sum_{i=1}^{N} |P_{3D}(\mathbf{u} + \mathbf{u}_{\text{in},i})|^2 + \beta} - \hat{O}(\mathbf{u}) \right]. \tag{4}$$

N stands for the number of all the illumination angles used, including both coherent and partially coherent illumination. $\hat{O}(\mathbf{u})$ and $\hat{O}^{\text{new}}(\mathbf{u})$ respectively represent the object's scattering potential spectrum before and after the update. α is the update weight that controls the effective step size of the difference map iteration. An excessively large value may cause numerical instability, whereas an overly small value leads to slow convergence. Here, α was set to 0.2 to balance numerical stability and convergence speed. β is a regularization parameter used for noise suppression, which was set to 0.001 to effectively suppress noise while preserving low-frequency structural components of the sample. $\hat{O}_i^{\text{new}}(\mathbf{u})$ is the 3D sub-spectrum with intensity constraints at a certain illumination angle, which can be obtained by mapping the updated 2D first-order scattered field $\hat{U}_{s1,i}^{\text{new}}(\mathbf{u}_T)$ to the 3D Ewald sphere (see Sec. 4). The strategy of differential map serves as a global optimization algorithm aimed to update the entire scattering potential in one iteration, which is beneficial to convergence and robustness against noise. Considering the ill-posedness caused by the unavoidable missing-cone problem,[46] we further incorporated a spatiotemporal continuity prior for biological structures across the $x-y-z-t$ domain as physical constraints to guide the RI reconstruction.[43] The last two items in Eq. (3) introduce the spatiotemporal total variation (TV) regularization, which is based on the knowledge of biological structures' piecewise spatial smoothness and temporal consistency. $D_{xyz}(\cdot)$ and $D_t(\cdot)$ denote the finite difference operators along the spatial and temporal dimensions, respectively, whereas parameters τ_{xyz} and τ_t control the strength of the regularization. To balance artifact suppression and detail preservation in both spatial and temporal domains and to enforce temporal continuity without oversmoothing rapid dynamic changes, τ_{xyz} was set to 1×10^{-4} and τ_t was set to 5×10^{-5} (see Note 4 in the Supplementary Material).

Using unstained live PLC cells as an example, Fig. 1(d) illustrates the spatiotemporal collaborative tomographic reconstruction workflow of STM-FPDT. A series of intensity stacks for 3D RI reconstruction per frame can be continuously collected at an imaging speed of 5 Hz by repeating the LED illumination process according to the designed timing sequence (see Sec. 4). Full algorithmic details and pseudocode are available in Sec. 4 and Note 3 in the Supplementary Material. Thanks to the physically intensity constraints, effective initialization, sufficient data redundancy, and additional regularization priors, the STM-FPDT reconstruction algorithm demonstrates stable and efficient convergence.

2.2 Motion Blur Impact on Living Cell Imaging Quality

In dynamic 3D imaging of live cells, motion blur artifacts caused by cellular movement severely degrade tomographic image quality, particularly in conventional systems requiring prolonged data acquisition times. These artifacts obscure rapid subcellular dynamic events and hinder the accurate observation of cellular physiological processes. The proposed STM-FPDT alleviates this issue by adopting a hybrid C/PC annular illumination strategy and a spatiotemporal collaborative reconstruction framework. By encoding the scattered field information from 45 illumination angles into only 11 measurements, STM-FPDT significantly improves acquisition speed, which is the primary contributor to motion-blur mitigation. The sliding window protocol and spatiotemporal regularization in the reconstruction framework further smoothed the artifacts and improved the reconstruction quality (see Note 5 and Fig. S6 in the Supplementary Material). To demonstrate this point, we implemented the tomographic imaging of unstained living PLC cells and compared the results of our technique with those of three existing reconstruction strategies (Fig. 2). By promptly switching between the four illumination strategies, we can achieve data acquisition of four reconstruction strategies in adjacent time, which are FPDT[27] with 45 illumination angles, annular intensity diffraction tomography (aIDT)[47] with 45 illumination angles, FPDT with 11 sparse illumination angles, and STM-FPDT with 11 measured images. The illumination schematics with the same theoretical spatial resolution are displayed in the first row in Fig. 2(b), whereas the corresponding acquisition time in experiments is compared in Fig. 2(c). Compared with conventional FPDT, STM-FPDT achieves the same spectral information with a 4.5-fold reduction in acquisition time.

The reconstructed results for two ROIs in Fig. 2(a) corresponding to four strategies are zoomed on in the second and third rows of Fig. 2(b), highlighting the effects of motion blur artifacts on organelles with different motion states. In general, smaller subcellular structures tend to move at a faster rate, and conversely, larger structures move slowly. Thus, we observe that for larger nucleoli, the reconstruction results of the conventional FPDT using 45 illumination angles and the proposed STM-FPDT have indistinguishable imaging quality. Meanwhile, the results obtained from FPDT with 11 illumination angles show a considerable RI underestimation problem attributed to the

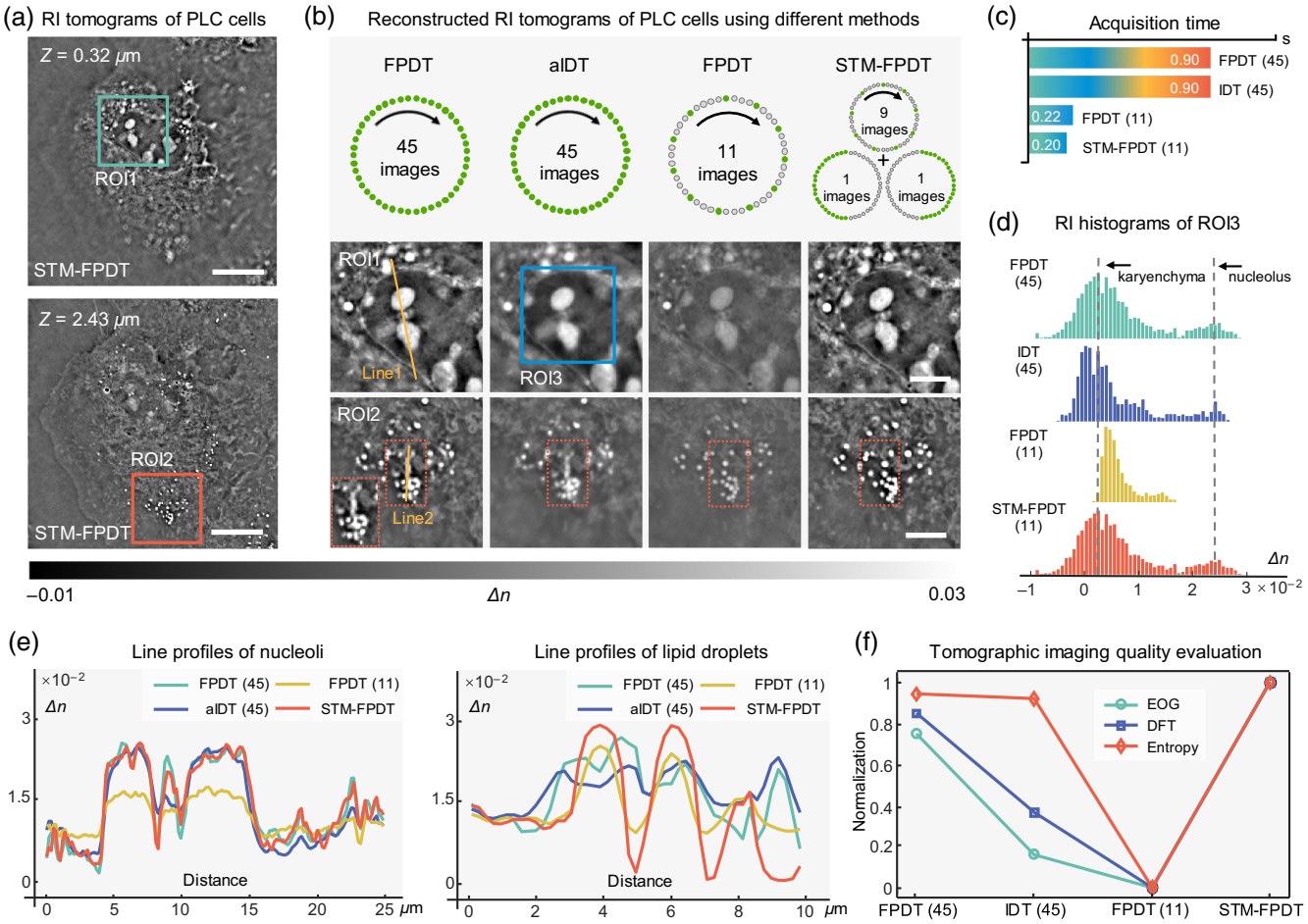

Fig. 2 Motion blur degrades the resolution in dynamic 3D imaging of live cells. (a) Reconstructed RI tomograms of living PLC cells at different depths using the proposed STM-FPDT technique. (b) Illumination schematic diagrams corresponding to the four diffraction tomography reconstruction strategies are shown in the first row. The second and third rows show the reconstructed RI tomograms of two ROIs in (a) using these diffraction reconstruction strategies with the same theoretical spatial resolution. (c) Comparison of data acquisition time of four different reconstruction strategies. (d) RI histograms of ROI3 corresponding to the four reconstruction results. (e) The corresponding line profiles are displayed to compare the effective imaging resolution of slow-motion nucleoli and rapid-motion lipid droplets in living cells [indicated by the yellow lines in (b), respectively]. (f) Three clarity evaluation functions (including EOG, DFT, and entropy) are used to assess the quality of 3D tomographic imaging under various reconstruction strategies, highlighting the superior imaging quality achieved by STM-FPDT. Scale bars: (a) 20 μm and (b) 10 μm.

inadequate acquisition of spectral information led by a limited number of illumination angles. In addition, the result of aIDT presents a slight blur compared to STM-FPDT due to the approximation assumption in the slice-wise deconvolution reconstruction process of aIDT. This phenomenon illustrates the advantages of the reconstruction strategy based on intensity self-consistency in terms of imaging quality and resolution. Four RI histograms of ROI3 corresponding to the various reconstruction results are compared in Fig. 2(d), which statistically verifies the above conclusions, since the fourth one is almost identical to the first one and outperforms the remaining two.

When focusing on the imaging of smaller structures such as lipid droplets [third row in Fig. 2(b)], STM-FPDT demonstrates significant advantages in alleviating motion blur artifacts due to rapid movement. The lipid droplets are clearly visible and distinguishable in the result of STM-FPDT, whereas in the other three cases, the lipid droplets exhibited varying degrees of motion blur artifacts and RI underestimation. Moreover, the RI line profiles across organelles are depicted in Fig. 2(e), further proving the above conclusions quantitatively. To quantitatively evaluate the imaging results, three clarity evaluation functions, including energy of gradient (EOG), discrete Fourier transform (DFT), and entropy (see Note 6 in the Supplementary Material for detailed descriptions and calculations), are used to assess the quality of 3D tomographic imaging under various reconstruction strategies. No matter which evaluation function is used, it is proven that the quality of 3D tomographic imaging of STM-FPDT outperforms, as shown in Fig. 2(f).

It is noteworthy that the imaging speed is limited by the current camera's exposure time. The utilization of higher-power LEDs allows for further enhancement of imaging speed by decreasing the camera's exposure time in partial readout mode. The comparative reconstruction results of fixed samples using STM-FPDT and aIDT under varying exposure times are presented in Note 7 and Fig. S7 in the Supplementary Material, demonstrating that the proposed STM-FPDT method achieves superior imaging quality and resolution compared to the conventional aIDT approach. Furthermore, in Note 8 and Fig. S8 in the Supplementary Material, we provide a theoretical analysis of the system's resolution, yielding a lateral resolution of 347 nm and an axial resolution of 1.54 μm. These values were experimentally validated through tomographic imaging of a phase resolution target and subcellular structures within PLC cells, confirming the method's high-resolution capabilities. Finally, we experimentally validate axial reconstruction performance using a resolution target and 3D-printed sample, demonstrating relatively reliable reconstruction of axial structures within an imaging depth of 15 μm (see Note 9, Figs. S9 and S10 in the Supplementary Material).

2.3 Visualization of Dynamics Associated with Plasma Membrane and Actin Filaments Contraction

The proposed STM-FPDT can meet the requirements for label-free dynamic 3D imaging of live-cells imaging with high spatiotemporal resolution, revealing fine structures and dynamics in cellular processes such as pinocytosis, exocytosis, and actin filament contraction. Figure 3 presents a detailed tomographic reconstruction and time-lapse analysis of PLC cells to reveal their dynamic 3D imaging features. Some black regions can be observed within the imaged cells [Fig. 3(a)], which are vesicles formed during the process of pinocytosis and exocytosis and have a lower RI than the surrounding medium due to the presence of internal voids. Pinocytosis and exocytosis are crucial cellular physiological processes in which vesicles serve as transport vehicles, enabling cells to internalize extracellular substances or to export intracellular materials to the extracellular environment. The RI distribution at different depths in Fig. 3(b) offers a 3D structure exploration of the vesicles and plasma membrane. Further, the temporal evolution of the RI distribution along a specified orange arrow over 23 min is presented in Fig. 3(c). This visualization effectively illustrates the fluctuations and folds in the plasma membrane during the pinocytosis and exocytosis process. As pinocytosis and exocytosis proceeded, the percentage composition of vesicles tended to decrease [Fig. 3(d)]. Continuing the time-lapse insights, Fig. 3(e) sequentially presents RI tomograms at different time points, demonstrating the dynamic process of pinocytosis and exocytosis (see Video 1). The fusion and dissipation processes of vesicles within the confined region indicated by the orange box in Fig. 3(e) are emphasized in Fig. 3(f). These findings hold significant promise in offering novel insights into biological phenomena such as intracellular trafficking and metabolic regulation.

An additional square area from Fig. 3(a) at the z plane of 1.60 μm and the time point of 26:51 is enlarged in Fig. 3(g), which reveals the actin filaments within filopodia at the cell boundary. This level of detail underscores the superior imaging resolution of our technique. Figure 3(h) further highlights subcellular structure changes at different time points, showcasing the phenomenon of actin filament contraction (see Video 2). The second row focuses on a small box, providing a magnified view that distinctly captures filament rupture at the point of 12:14. To characterize the accuracy of RI imaging with STM-FPDT, we performed 200 measurements of the same background region. By fitting the histogram with a Gaussian function and analyzing the box plot, we demonstrated the RI imaging precision of 1.18×10^{-3} [Figs. 3(i) and 3(j)]. In addition, a Gaussian function also was used to fit the RI profiles of lines orthogonal to actin filaments with 100 measurements. We found that the full width at half maximum (FWHM) of the actin filament measured by our STM-FPDT is approximately 610 nm [Figs. 3(k) and 3(l)].

2.4 Revealing the Dynamics of Mitochondria Interacting with Other Organelles

Mitochondria serve as the hub of oxidative metabolism in eukaryotes, supplying essential energy for cells through oxidation. Their morphological and quantitative changes are closely related to cellular metabolism activity. Figure 4 depicts the elongated mitochondria in PLC cells and their dynamic interactions with other organelles. A subregion of the reconstructed tomogram of a cell at 0 μm z plane is shown in Fig. 4(a). The ROI1 is zoomed at various time points to provide a clear view of the dynamic progression of mitochondrial fission multiplication [Fig. 4(b)]. During fission, the mitochondria elongate bilaterally, forming a thin neck in the middle [arrow in Fig. 4(b)], and then split in two to produce new mitochondria. This dynamic process is also animated in Video 3. By analyzing the RI profile across the point A overtime in Fig. 4(b), we can effectively monitor the phenomenon of mitochondrial fission at the point of 10:42 [Fig. 4(c)]. In addition, the width of mitochondria can be quantified using the RI line profile, with a diameter of 746 nm, consistent with the general theoretical interval of 0.5 to 1.0 μm.

Furthermore, three representative ROIs from Fig. 4(e) are magnified in Figs. 4(f)–4(h) to show detailed dynamic processes of subcellular structures at various time points. ROI2 vividly captures morphological changes in mitochondria, highlighting a dynamic shift from elongated to crimped shapes over time [arrow in Fig. 4(f)]. Their morphological and quantitative changes are closely related to cellular metabolism activity. Figure 4(g) provides a clear illustration of intracellular interactions between lipid droplets and the mitochondrial in ROI3, where lipid droplets dynamically engage and move along the mitochondria. This interaction may contribute to lipid transfer and energy metabolism, as lipid droplets serve as the main energy storage source in cells, and lipids in them can be transported into mitochondria to provide energy substances. Moreover, Fig. 4(h) depicts a representative example of the evolving interaction between vesicles and mitochondria over time. The region emphasized by the orange arrow reveals the rotational dynamics and morphological transformations of vesicles at different time points, culminating in the encapsulation of a vesicle by adjacent mitochondria (see Video 4). We speculate that during this process, macromolecular substances may be transported into or out of mitochondria via vesicles to maintain mitochondrial function and internal homeostasis, playing a crucial role in regulating cell metabolism.

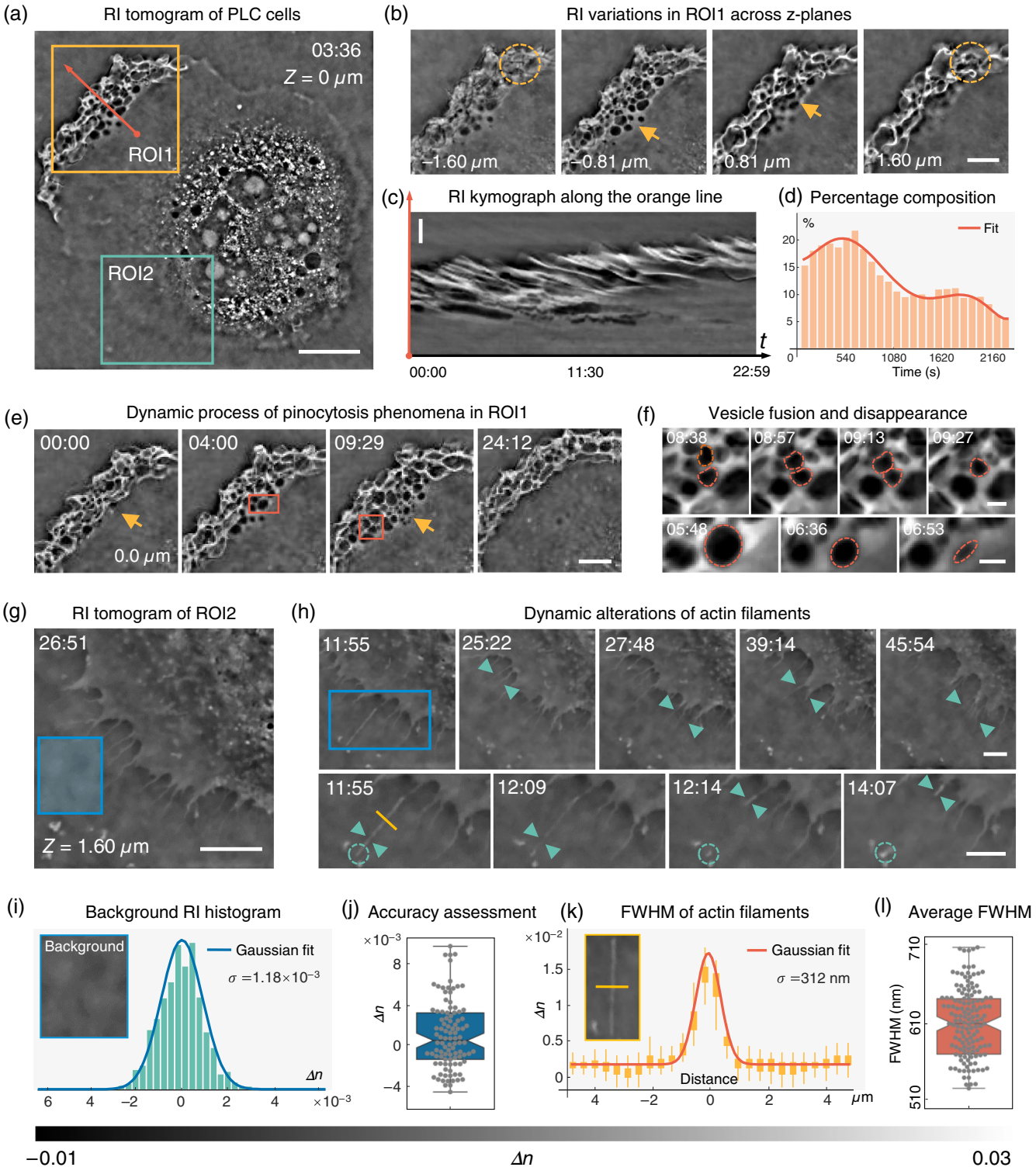

Fig. 3 Visualization of the plasma membrane blebbing and actin dynamics of PLC cells. (a) Reconstructed RI distributions of PLC cells at 0 μm z plane at the point of 03:36. (b) RI results at four different depths within the yellow square box in (a). The black region pointed out by the arrows represents vesicles formed during the pinocytosis and exocytosis process of the plasma membrane, with an RI lower than the medium, containing internal cavities. (c) Kymograph along the orange line arrow direction in (a) showing fluctuations and folds in the plasma membrane during the pinocytosis and exocytosis process. (d) Area percentage of vesicles at different time points within the yellow square box in (a). (e) Visualization of pinocytosis and exocytosis phenomena at different time points (see also Video 1). (f) Representative examples of vesicle fusion and disappearance events. (g) Clear observation of actin filaments at the cell boundary

Fig. 3 (*Continued*) at $z = 1.60$ μm. (h) Visualization of changes in actin filaments at different time points. The second row shows the phenomenon of filament rupture at the point of 12:14 (see also Video 2). (i) RI histogram of the background region in the reconstructed images and Gaussian fitting curve distribution. RI imaging precision of STM-FPDT is 1.18×10^{-3} according to the standard deviation obtained by Gaussian fitting. (j) Average RI imaging accuracy measured at 200 different time points. (k) Average RI distribution of lines orthogonal to actin filaments (at 100 time points with almost the same actin filament). (l) The average FWHM value of profiles orthogonal to actin filaments marked in (k) measured at 100 time points is about 610 nm. Scale bars: (a) 20 μm, (b), (e), (g) 10 μm, (c), (h) 5 μm, and (f) 2 μm (Video 1, MP4, 5.82 MB [URL: https://doi.org/10.1117/1.AP.8.2.026003.s1]; Video 2, MP4, 5.14 MB [URL: https://doi.org/10.1117/1.AP.8.2.026003.s2]).

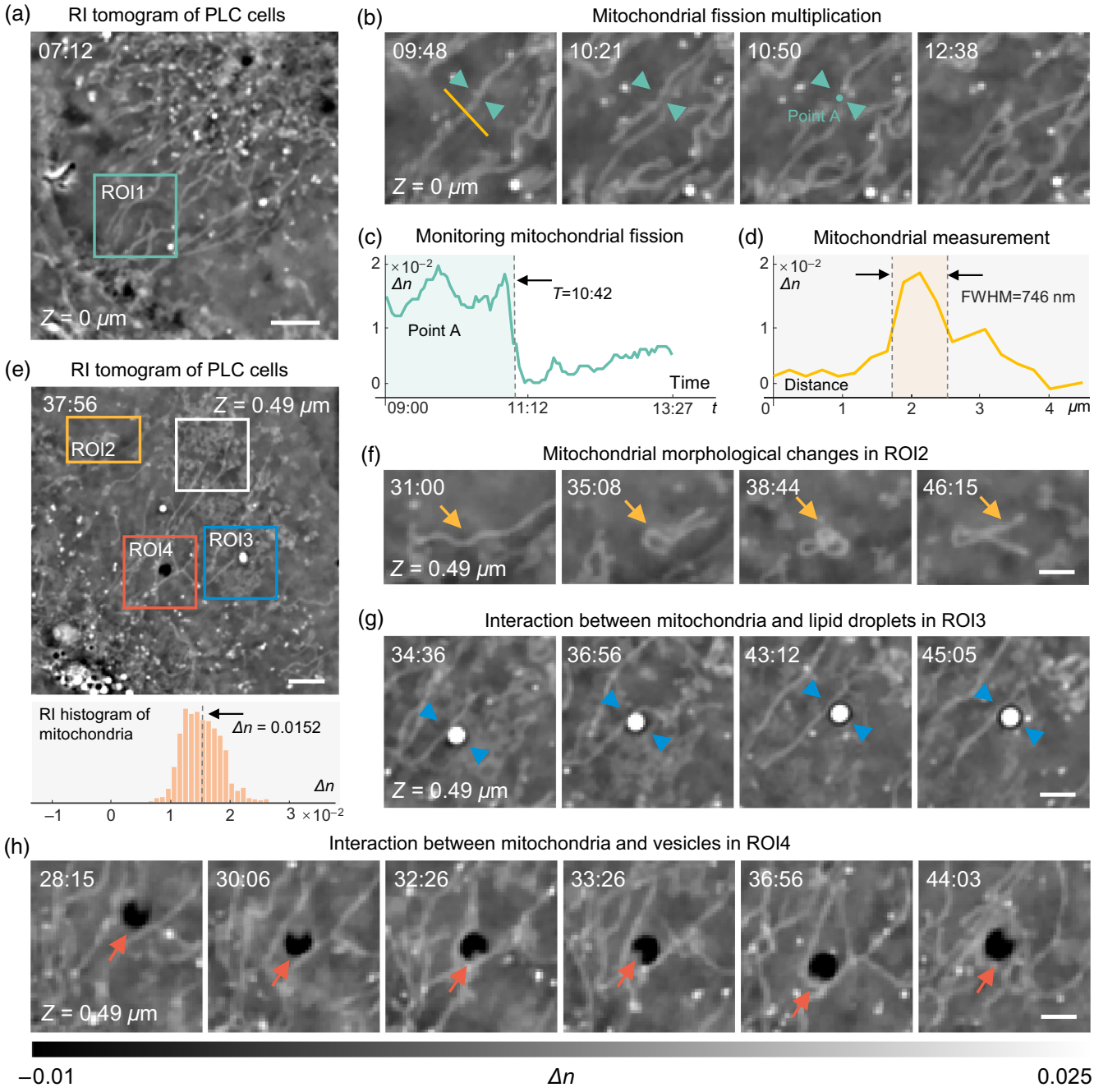

Fig. 4 Visualization of mitochondria dynamics of PLC cells. (a) Reconstructed magnified region of the RI distributions at 0 μm z plane at the time point of 07:12. (b) RI tomograms at different time points within the green square box in (a), offering a clear view of the dynamic progression of

Fig. 4 (*Continued*) mitochondrial fission multiplication. (c) RI line profile across point A in (b) from time point 9:00 to 13:27, effectively monitoring the phenomenon of mitochondrial fission at the point of 10:42 (see also Video 3). (d) RI line profile across mitochondria reveals its diameter of 746 nm, providing quantitative insights into the dynamics of mitochondria. (e) Another subregion of RI tomogram at 0.49 μm z plane and histogram corresponding to the white box region. (f) Visualization of morphological change of the mitochondria within the yellow rectangular box in (e). (g) and (h) Representative examples of intracellular interactions of mitochondria with lipid droplets and vesicles within the blue and orange square boxes in (e), respectively (see also Video 4). Scale bars: (a), (e) 5 μm, and (b), (f)–(h) 2 μm (Video 3, MP4, 4.54 MB [URL: https://doi.org/10.1117/1.AP.8.2.026003.s3]; Video 4, MP4, 6.94 MB [URL: https://doi.org/10.1117/1.AP.8.2.026003.s4]).

2.5 Monitoring Lipid Droplet Trajectories and Analyzing Intercellular Interactions

Lipid droplets, recognized as storage depots for lipids, have garnered significant attention for their intricate involvement in cellular processes, particularly in the investigation of diseases such as obesity and cancer. They are well characterized in hepatocytes such as PLC cells due to their high lipid content. Figure 5 presents clear tomographic results of PLC cells, along with monitoring and analysis of lipid droplets' trajectories and intercellular interactions. The RI distribution at distinct axial planes is showcased in Fig. 5(a), illustrating discernible disparities in cellular structures across each plane against an artifact-free background, with all lipid droplets clearly visible. Remarkably, the proposed method enables precise spatial localization and trajectory tracking of organelles, owing to excellent spatiotemporal resolution. Figures 5(b) and 5(c) demonstrate the efficacy of our technique by capturing the dynamics of sparsely distributed lipid droplets inside cells. Five lipid droplets, each 1.5 μm in diameter, are simultaneously located and tracked, which distinctly reveals their position at different time points and uninterrupted trajectories. The detailed organelle tracking algorithm can refer to Note 11 and Fig. S10 in the Supplementary Material. The visualization of the whole dynamically continuous process is given in Video 5. In the selected subregion, the high-contrast nucleolus and lipid droplets, as well as well-defined nuclear membrane boundaries, enable it to be clearly delineated, facilitating subsequent feature extraction for precise organelle segmentation [Fig. 5(d)]. Moreover, we can extend the utility of STM-FPDT to dynamic monitoring and statistical analysis of cellular state. The average concentration distribution of lipid droplets along the z-axis measured at 100 time points is shown in Fig. 5(e), demonstrating their 3D spatial distribution inside cells. In addition, the percentage content of lipid droplets and volume of cells changed over time, providing further insights into cellular processes such as metabolism, energy reserves, and signal transduction [Figs. 5(f) and 5(g)].

Finally, the method also allowed us to study intercellular interactions, including the communication between neighboring cells during growth and division. We demonstrate this phenomenon by exhibiting four PLC cells after completing division in Fig. 5(h). Figure 5(i) presents the time-lapse imaging result corresponding to the orange box in Fig. 5(h), capturing the nuanced dynamics of cell membrane contraction and expansion [orange arrows in Fig. 5(i)], along with mitochondrial migration between cells via membrane fusion [blue circles in Fig. 5(i)]. As membrane fusion progresses, the boundary between adjacent cells becomes increasingly blurred, facilitating the intercellular migration of filamentous mitochondria. After ~21 minutes, mitochondrial migration is completed, followed by a gradual contraction of mitochondrial morphology and a concomitant re-establishment of clearer cell boundaries (see also Video 6). Additional experimental results related to cell migration over a period of two hours are presented in Note 11 and Fig. S12 in the Supplementary Material, and Video 7, revealing that cell movement is achieved through the continuous adhesion, contraction, and depolymerization process between cells and the extracellular matrix. Cell migration underlies key physiological and pathological processes, including immune responses, tissue repair, and tumor metastasis. Using the proposed STM-FPDT technique, elucidating cell migration mechanisms may uncover disease origins and progression while informing therapeutic and drug development strategies (Video 7, MP4, 13.1 MB [URL: https://doi.org/10.1117/1.AP.8.2.026003.s7]).

3 Summary and Discussion

In this study, we have demonstrated STM-FPDT, a motion-free, noninterferometric ODT technique tailored for high-speed, label-free 3D imaging of live cells. This technique theoretically extends traditional ODTs' spatial coherent imaging mechanism to a C/PC hybrid imaging scheme. The developed NA-matched annular C/PC hybrid illumination strategy preserves phase contrast in the measurement data while enabling parallel spectral acquisition, substantially reducing the number of required intensity images. The theoretical effort goes in parallel with a spatiotemporal cooperative tomographic reconstruction framework designed to solve the inverse scattering problem. By integrating a sliding window protocol with nonlinear global optimization, this framework effectively eliminates motion artifacts by leveraging the spatiotemporal continuity prior of biological structures in the $x-y-z-t$ domain.

Longitudinal monitoring experiments of PLC cells demonstrated the STM-FPDT's capability for 3D tomographic imaging at 5 Hz volumetric rates with 347 nm lateral/1.54 μm axial resolution, revealing sub-second organelle dynamics including membrane blebbing, cytoskeletal fiber fluctuations, and mitochondrial fission. Due to its straightforward compatibility with standard bright-field microscopes, this technique provides a widely accessible platform for quantitative, high-spatiotemporal-resolution studies of live-cell physiology, addressing the growing demand for imaging rapid cellular dynamics in their native physiological state. In the future, advances in deep learning and neural network-based reconstruction frameworks[48] are expected to further enhance STM-FPDT by enabling more efficient exploitation of spatiotemporal correlations improving robustness to noise and model mismatch. In particular, the integration of physics-informed neural networks[49] or hybrid model-driven and data-driven strategies[50] may allow adaptive

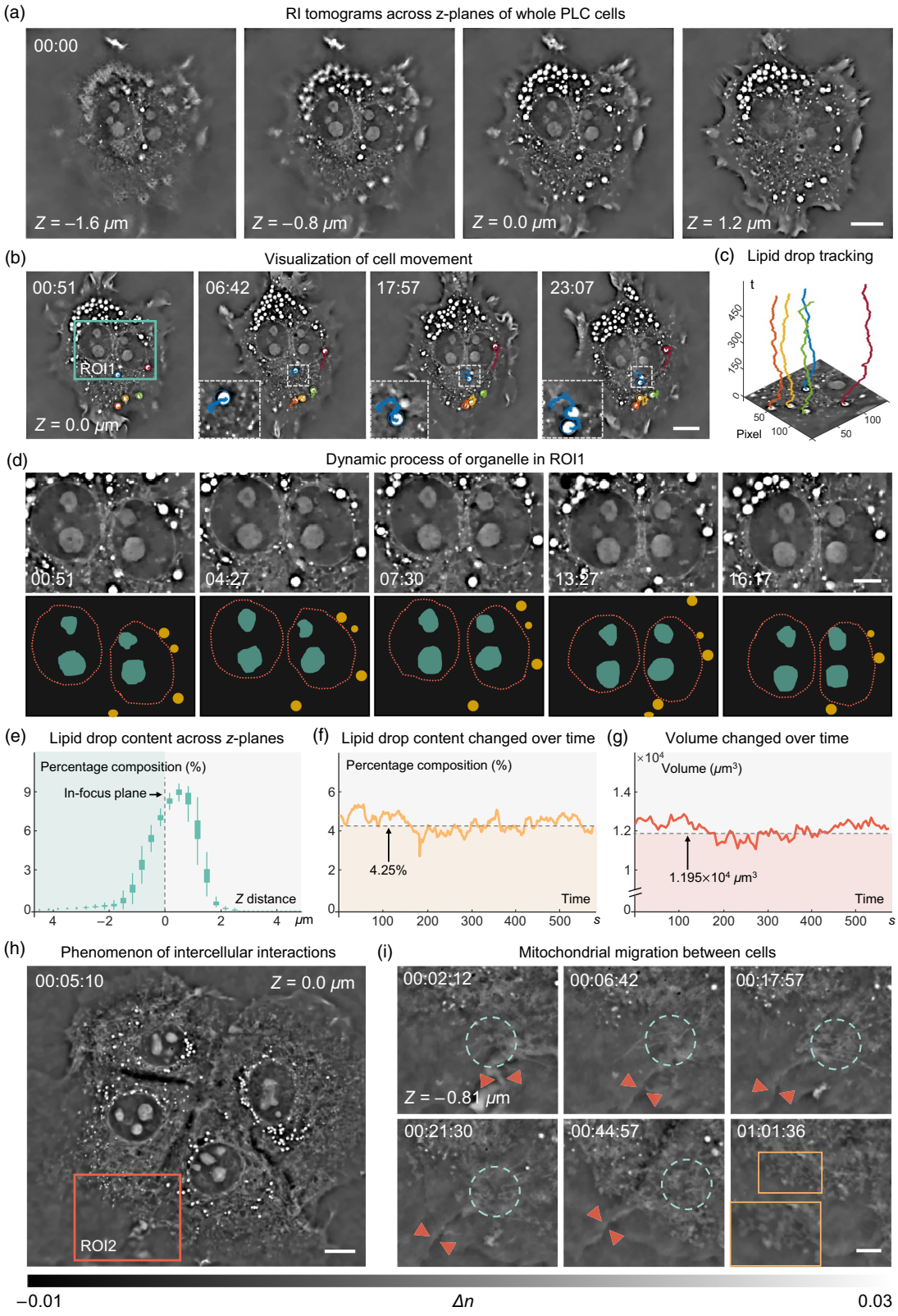

Fig. 5 Visualization of the tracking of lipid droplets and the intercellular interactions. (a) Reconstructed RI tomograms of PLC cells at four different z planes at the start time point of 00:00. (b), (c) Visualization of cell movement at different time points. Five sparsely distributed lipid droplets with a diameter of 1.5 μm inside cells are simultaneously located and tracked (see also Video 5). (d) The subcellular structures focused on the cell nucleus within the green box in (b) are enlarged in the first row, while the corresponding schematic diagrams highlight

Fig. 5 (*Continued*) the distributions of the nuclear membrane (orange), nucleolus (green), and lipids (yellow). (e) The average concentration distribution of intracellular lipid droplets along the *z*-axis was measured at 100 different time points. (f) Percentage content of lipid droplets inside cells changed over time. (g) The volume of cells changed over time. (h) Representative examples of intercellular interactions. The tomogram contains 4 bonded PLC cells. (i) Visualization of intercellular interactions at different time points within the orange square box in (h) showing the mitochondrial migration between cells by means of membrane fusion and fission (see also Video 6). Scale bars: (a), (b), (h) 10 μm, and (d), (i) 5 μm (Video 5, MP4, 3.80 MB [URL: https://doi.org/10.1117/1.AP.8.2.026003.s5]; Video 6, MP4, 8.42 MB [URL: https://doi.org/10.1117/1.AP.8.2.026003.s6]).

regularization, improved handling of rapid dynamic phase fluctuations, and more efficient reconstruction under extreme space-time bandwidth constraints. Moreover, fluorescence-assisted STM-FPDT[51,52] and polarization-sensitive STM-FPDT[53,54] are anticipated to integrate the molecular specificity of fluorescence or the intrinsic anisotropic properties of the sample with the noninvasiveness of diffraction tomography to provide deeper insights into investigating biological processes.

4 Appendix: Methods

4.1 Forward Intensity-Formation Model

ODT aims to reconstruct the scattering potential of a thick 3D object, which relates the spatial RI information of interest, defined as

$$O(\mathbf{r}) = k_0^2[n^2(\mathbf{r}) - n_m^2], \tag{5}$$

where $\mathbf{r} = (\mathbf{r}_T, z) = (x, y, z)$ is a shorthand notation for the 3D spatial coordinate. $k_0 = 2\pi/\lambda$ is the wavenumber with λ being the illumination wavelength in free space. $n(\mathbf{r})$ and n_m are the spatial RI distribution of the sample and its surrounding medium. When the object is illuminated by a plane wave $U_{\text{in}}(\mathbf{r})$, the scattered field $U_s(\mathbf{r})$ obeys the inhomogeneous wave equation:

$$(\nabla^2 + k_m^2)U_s(\mathbf{r}) = -O(\mathbf{r})U(\mathbf{r}), \tag{6}$$

where $k_m = k_0 n_m$ is the wavenumber in the medium, and ∇^2 is 3D Laplacian operator. $U(\mathbf{r})$ represents the total transmitted field that is written as the superposition of the incident field and the scattered field:

$$U(\mathbf{r}) = U_{\text{in}}(\mathbf{r}) + U_s(\mathbf{r}). \tag{7}$$

Further, we can obtain the following linear relation between the first-order scattered field $U_{s1}(\mathbf{r})$ and the object function $O(\mathbf{r})$ in the Fourier space by employing Green's function[55]:

$$\hat{O}(\mathbf{u} - \mathbf{u}_{\text{in}}) = 4\pi j u_z \hat{U}_{s1}(\mathbf{u}_T) P_{3\text{D}}(\mathbf{u}), \tag{8}$$

where $\mathbf{u} = (\mathbf{u}_T, u_z) = (u_x, u_y, u_z)$ represents the 3D spatial frequency coordinates corresponding to $\mathbf{r}$ and $\mathbf{u}_{\text{in}}$ is the 3D incident plane wave vector. $\hat{O}(\mathbf{u})$ and $\hat{U}_{s1}(\mathbf{u}_T)$ correspond to the 3D and 2D Fourier transforms of $O(\mathbf{r})$ and $U_{s1}(\mathbf{r}_T)$, respectively. $P_{3\text{D}}(\mathbf{u}) = P(\mathbf{u}_T)\delta(u_z - \sqrt{u_m^2 - |\mathbf{u}_T|^2})$ is defined as the 3D coherent transfer function, whose spectrum support is a restricted Ewald sphere limited by the objective's aperture function $P(\mathbf{u}_T)$.[56] With a specific incident illumination $\mathbf{u}_{\text{in}}$, the $U_{s1}(\mathbf{r})$ can be calculated from $O(\mathbf{r})$ using Eq. (8). Then, we can further establish the relationship between $U_{s1}(\mathbf{r})$ and $U(\mathbf{r})$ under the first-order Rytov approximation[57,58] and obtain the 2D intensity information corresponding to the current illumination

$$\begin{aligned} I_c(\mathbf{r}_T) &= |U(\mathbf{r}_T, \mathbf{u}_{\text{in}})|^2 \\ &= |U_{\text{in}}(\mathbf{r}_T, \mathbf{u}_{\text{in}}) \exp[U_{s1}(\mathbf{r}_T)/U_{\text{in}}(\mathbf{r}_T, \mathbf{u}_{\text{in}})]|^2. \end{aligned} \tag{9}$$

This is the intensity-formation process under coherent illumination, whereas the intensity distribution under partially coherent illumination is the incoherent superposition of coherent intensity, written as

$$\begin{aligned} I_{\text{pc}}(\mathbf{r}_T) &= \sum_{l=1}^{L} |U_l(\mathbf{r}_T, \mathbf{u}_{\text{in},l})|^2 \\ &= \sum_{l=1}^{L} |U_{\text{in},l}(\mathbf{r}_T, \mathbf{u}_{\text{in},l}) \exp[U_{s1,l}(\mathbf{r}_T)/U_{\text{in},l}(\mathbf{r}_T, \mathbf{u}_{\text{in},l})]|^2, \end{aligned} \tag{10}$$

where L is the number of discrete plane waves under partially coherent illumination.

4.2 Hardware Implementation

To realize dynamic 3D live-cell imaging with spatiotemporal-multiplexed Fourier ptychographic diffraction tomography, we constructed the experimental configuration based on a commercial inverted microscope (IX83, Olympus,Tokyo, Japan) equipped with a programmable annular LED illumination source (WS2812B, SMD-5050 Adafruit, New York City, United States). The illumination source, comprising 45 LED elements, is positioned 49 mm away from the sample stage to provide quasi-monochromatic illuminations (center wavelength 520 nm, with an FWHM of 18 nm). The illumination NA of 0.75 is carefully matched to the NA of the objective lens (40×/0.75 UPLSAPO, Olympus). Each LED element is precisely controlled by an ARM controller (MIMXRT1062, Teensy 4.1, NXP Semiconductors, Colorado, United States) to illuminate according to the designed timing sequence [Fig. 1(c)]. To facilitate time-lapse imaging of living cells, an incubation chamber (Tokai Hit INUF-IX3W, Japan) is incorporated between the illumination unit and detection objective. This chamber maintains an internal temperature of 37°C and provides a humidified atmosphere with 5% carbon dioxide. Furthermore, we employ an sCMOS camera (ORCA-Flash 4.0 C13440, Hamamatsu, pixel pitch 6.5 μm, pixel resolution 2048 × 2048) to record raw intensity images for label-free tomographic imaging of cells.

4.3 Data Acquisition

We group the 45 LED elements on a programmable annular array into the five sets of the nine equally spaced LED elements. For the data collection of the first frame, we first sequentially fire the first set of the nine equally spaced LEDs from the first set of LEDs. Each illumination lasts for 20 ms, which is precisely synchronized to the camera exposure for 20 ms. We then acquired a set of two partially coherent intensity images with 10 ms exposure time per frame using asymmetric semi-ring illumination from the 22 and 23 LEDs, respectively. For the data collection of the second frame, sequential illumination by the second set of nine LED elements, with the starting LED positioned anti-clockwise next to the ones on the first set of the nine LED elements, is responsible for coherent illumination. Similarly, the semi-annular illuminations, with the starting LED element being accordingly shifted anti-clockwise by five positions, are responsible for asymmetrically partially coherent intensity recording. With the 45 LED elements shown in Fig. S2 in the Supplementary Material encoded counterclockwise from 1 to 45, Table S1 in the Supplementary Material details the illumination groups and their corresponding timing sequence for the 11 images captured in each frame. This design takes advantage of the fast switching ability of LED elements on the programmable annular array and allows for parallel acquisition of scattering information from samples under all 45 different illumination angles, significantly expediting the data acquisition process. After repeating this process five times, the selected LED elements exhibited the same distribution as in the first frame. By repeating this precisely designed LED illumination sequence, STM-FPDT can continuously acquire a series of intensity stacks for 3D RI reconstruction at an imaging rate of 5 Hz per frame.

4.4 Reconstruction Algorithm

We developed a spatiotemporal collaborative reconstruction framework for STM-FPDT to achieve stable RI reconstruction. This framework integrates a sliding window protocol and nonlinear global optimization. For the $t+1$ frame tomographic imaging, the process can be described as follows, alternating between the spatiotemporal and Fourier domains.

Step 1: **Initialization.** Make an initial guess of the current frame's 3D spectrum $\hat{O}_{t+1}(\mathbf{u})$ using the reconstructed scattering potential spectrum from the previous frame $\hat{O}_t(\mathbf{u})$.
Step 2: **Intensity estimation.** Select a specific illumination angle $\{\mathbf{u}_{\mathrm{in},i}|i=1,2,\ldots,N\}$ to obtain the low-resolution 2D first-order scattered field spectrum $\hat{U}_{s1,i}(\mathbf{u}_T)$ according to

$$\hat{U}_{s1,i}(\mathbf{u}_T)=\frac{1}{4\pi j u_z}\hat{O}_{t+1}(\mathbf{u}-\mathbf{u}_{\mathrm{in},i})P_{3\mathrm{D}}(\mathbf{u}). \tag{11}$$

Upon converting the estimated $\hat{U}_{s1,i}(\mathbf{u}_T)$ to the spatial domain, the intensity can be determined subsequently in accordance with Eq. (9). By traversing all the illumination angles, we obtain the intensity stack $\{I_{c,i}(\mathbf{r}_T)|i=1,2,\ldots,N\}$ under coherent illumination. Then, based on the current set of light source distributions of partially coherent illumination, this intensity stack can be utilized to generate the partially coherent light intensity estimates $\{I_{\mathrm{pc},v}(\mathbf{r}_T)|v=1,2\}$ according to Eq. (10).
Step 3: **Intensity constraint.** Enforce the intensity constraint to $\hat{U}_{s1,i}(\mathbf{u}_T)$ to update the first-order scattered field $\hat{U}^{\mathrm{new}}_{s1,i}(\mathbf{u}_T)$. Note that the update formula includes both coherent and partially coherent illumination cases. For coherent illumination, the update equation is given by

$$U^{\mathrm{new}}_{s1,w}=U_{\mathrm{in},w}\ln\left[\sqrt{\frac{I^m_{c,w}}{I_{c,w}}}\exp(U_{s1,w}/U_{\mathrm{in},w})\right],\quad w=1,2,3,\ldots,W, \tag{12}$$

where $w\in\{i=1,2,\ldots,N\}$ is the coherent illumination angle, and $I^m_{c,w}$ is the measured intensity under the corresponding illumination. W is the number of coherent imaging. For partially coherent illumination, the update formula is given by

$$U^{\mathrm{new}}_{s1,l}=U_{\mathrm{in},l}\ln\left[\sqrt{\frac{I^d_{c,l}}{I_{c,l}}}\exp(U_{s1,l}/U_{\mathrm{in},l})\right],\quad l=1,2,3,\ldots,L, \tag{13}$$

where $l\in\{i=1,2,\ldots,N\}$ is discrete illumination angle under partially coherent illumination, and $I^d_{c,i}$ is the decomposed intensity image from the measured intensity $I^m_{\mathrm{pc},v}$:

$$I^d_{c,l}=|U_{\mathrm{in},l}\exp(U_{s1,l}/U_{\mathrm{in},l})|^2\frac{I^m_{\mathrm{pc},v}}{I_{\mathrm{pc},v}}. \tag{14}$$

Note that the two partially coherent intensity images can theoretically access all aperture information, but the additional coherent intensity images captured in the experiment are to ensure sufficient data redundancy, guaranteeing the correctness of the spectral de-multiplexing process.
Step 4: **Spectrum update.** Integrate the updated 2D first-order scattered field spectrum under all illumination $\{U^{\mathrm{new}}_{s1,i}|i=1,2,\ldots,L\}$, and map them onto 3D coordinates to obtain $\{O^{\mathrm{new}}_i|i=1,2,\ldots,L\}$. Then update the scattering potential spectrum according to Eq. (4) to obtain $\hat{O}^{\mathrm{new}}_{t+1}(\mathbf{u})$. Perform the inverse Fourier transform of this updated scattering potential to get $O^{\mathrm{new}}_{t+1}(\mathbf{r})$.
Step 5: **Spatiotemporal continuity constraint.** Calculate the cost function $\ell(O^{\mathrm{new}}_{t+1})$ based on Eq. (3), where spatiotemporal TV regularization is expressed as, $D_{xyz}(O^{\mathrm{new}}_{t+1})=\sum\sqrt{(\nabla_x O^{\mathrm{new}}_{t+1})^2+(\nabla_y O^{\mathrm{new}}_{t+1})^2+(\nabla_z O^{\mathrm{new}}_{t+1})^2}$ and $D_t(O^{\mathrm{new}}_{t+1})=\sum\sqrt{(O^{\mathrm{new}}_{t+1}-O^{\mathrm{new}}_t)^2}$. Then update the scattering potential in the spatial domain using the proximal gradient method[59] based on this cost function.
Step 6: **RI reconstruction.** Repeat Step 2 to Step 5 until the cost function falls below the set threshold, i.e., $\ell(O^{\mathrm{new}}_{t+1})\le\varepsilon$, indicating that $O_{t+1}(\mathbf{r})$ has converged. The 3D spatial RI distribution of the sample can be obtained according to the following relationship:

$$n_{t+1}(\mathbf{r})=\sqrt{\frac{1}{k_0^2}O_{t+1}(\mathbf{r})+n_m^2}. \tag{15}$$

4.5 Coverslip Preparation

The coverslips (Cat. No. YA0351, Solarbio) intended for fixation cell imaging underwent pre-cleaning procedures. Initially, they were submerged in a 10% powdered precision ultrasonic

cleaner (Branson, B200, Brookfield, United States) and sonicated for 10 min. After rinsing with deionized water, the coverslips then underwent sonication in acetone for 15 min, followed by an additional sonication in 1 mol/L NaOH for 10 min. Subsequently, the coverslips were rinsed again with deionized water and subjected to three rounds of sonication, each lasting at least 5 min. Finally, the cleaned coverslips were stored in an alcohol solution with a concentration greater than 95% at 4°C.

4.6 Cell Preparation

For unstained HeLa cell fixation, precleaned coverslips were initially positioned within a 12-Well Cell Culture Cluster (Costar 3513, Corning). HeLa cells were then seeded into a culture medium consisting of 90% RPMI Medium1640 basic media, 10% fetal bovine serum (FBS), and 1% penicillin/streptomycin (all Gibco, Thermo Fisher Scientific, Waltham, Massachusetts, United States). The HeLa cells were subsequently cultured at 37°C in a humidified atmosphere containing 5% carbon dioxide for several hours until reaching ∼50% confluency. Upon reaching this threshold, the coverslips were removed from the culture cluster, rinsed twice with phosphate buffered saline (PBS), and exposed to pre-warmed fixation buffer (MTSB with a 4% paraformaldehyde) for 10 minutes at room temperature. Finally, the coverslips underwent three rinses with 1× PBS and DI water before being affixed to microscope slides. Following these procedures, HeLa cells were successfully sealed between the microscope slide and coverslip for subsequent tomographic imaging.

For PLC cells, an initial density of 200 cells/cm^2 were seeded in a glass bottom cell culture dish (Cat. No.: 801002, 15 mm glass diameter) using high-glucose DMEM (containing 110 mg/L sodium pyruvate, 4.5 g/L D-glucose, and L-glutamine) supplemented with 1% penicillin/streptomycin and 10% FBS (all Gibco, Thermo Fisher Scientific). The cells were then incubated at 37°C in a humidified atmosphere with 5% carbon dioxide for 24 h to facilitate attachment. Following this incubation period, the cells were rinsed twice with PBS, and fresh pre-warmed medium was added. Subsequently, the cells were positioned in the incubation chamber for multihour dynamic 3D live-cell imaging.

Disclosures

The authors declare no conflicts of interest.

Code and Data Availability

The data that support the findings of this study are available from the corresponding author upon reasonable request.

Ethics Approval and Consent to Participate

All experimental procedures were approved by the Institutional Biosafety Committee at Nanjing University of Science and Technology.

Authors Contribution

C.Z. and S.Z. developed the theoretical description of the method; S.Z. performed experiments; S.Z. and Q.S. analyzed the data; C.Z., S.Z, and J.S. participated in discussions during the development of the paper; D.J., Q.C., and C.Z. conceived and supervised the research; all authors contributed to writing the paper.

Acknowledgments

This work was supported by the National Key Research and Development Program of China (Grant Nos. 2024YFE0101300, 2022YFA1205002, 2024YFF0505603, and 2024YFF0505600), and the National Natural Science Foundation of China (Grant Nos. 62227818, 62361136588, 62305162, U21B2033, 62505136, and 62575139). See Note 1–11, Figs. S1–S12 and Table S1 in the Supplementary Material and Videos 1–7 for supporting content.

References

1. N. Lane, "The unseen world: reflections on Leeuwenhoek (1677) 'concerning little animals'," *Philos. Trans. R. Soc. B Biol. Sci.* **370**(1666), 20140344 (2015).
2. H. Gest, "The discovery of microorganisms by Robert Hooke and Antoni van Leeuwenhoek, fellows of the Royal Society," *Notes Rec. R. Soc. Lond.* **58**(2), 187–201 (2004).
3. A. J. Wollman et al., "From animaculum to single molecules: 300 years of the light microscope," *Open Biol.* **5**(4), 150019 (2015).
4. J. Mertz, *Introduction to Optical Microscopy*, Cambridge University Press (2019).
5. S. W. Hell, "Far-field optical nanoscopy," *Science* **316**(5828), 1153–1158 (2007).
6. F. W. Rost, *Fluorescence Microscopy*, Vol. **2**, Cambridge Univeristy Press (1992).
7. J. W. Lichtman and J.-A. Conchello, "Fluorescence microscopy," *Nat. Methods* **2**(12), 910–919 (2005).
8. R. H. Webb, "Confocal optical microscopy," *Rep. Prog. Phys.* **59**(3), 427 (1996).
9. E. Betzig et al., "Imaging intracellular fluorescent proteins at nanometer resolution," *Science* **313**(5793), 1642–1645 (2006).
10. M. J. Rust, M. Bates, and X. Zhuang, "Sub-diffraction-limit imaging by stochastic optical reconstruction microscopy (STORM)," *Nat. Methods* **3**(10), 793–796 (2006).
11. M. G. Gustafsson, "Surpassing the lateral resolution limit by a factor of two using structured illumination microscopy," *J. Microsc.* **198**(2), 82–87 (2000).
12. J. Qian et al., "Structured illumination microscopy based on principal component analysis," *eLight* **3**(1), 4 (2023).
13. K. M. Dean and A. E. Palmer, "Advances in fluorescence labeling strategies for dynamic cellular imaging," *Nat. Chem. Biol.* **10**(7), 512–523 (2014).
14. L. Schermelleh et al., "Super-resolution microscopy demystified," *Nat. Cell Biol.* **21**(1), 72–84 (2019).
15. D. J. Stephens and V. J. Allan, "Light microscopy techniques for live cell imaging," *Science* **300**(5616), 82–86 (2003).
16. R. Hoebe et al., "Controlled light-exposure microscopy reduces photobleaching and phototoxicity in fluorescence live-cell imaging," *Nat. Biotechnol.* **25**(2), 249–253 (2007).
17. F. Zernike, "Phase contrast, a new method for the microscopic observation of transparent objects," *Physica* **9**(7), 686–698 (1942).
18. E. Cuche, F. Bevilacqua, and C. Depeursinge, "Digital holography for quantitative phase-contrast imaging," *Opt. Lett.* **24**(5), 291–293 (1999).
19. P. Gao et al., "Phase-shifting Zernike phase contrast microscopy for quantitative phase measurement," *Opt. Lett.* **36**(21), 4305–4307 (2011).
20. E. Cuche, P. Marquet, and C. Depeursinge, "Simultaneous amplitude-contrast and quantitative phase-contrast microscopy by numerical reconstruction of Fresnel off-axis holograms," *Appl. Opt.* **38**(34), 6994–7001 (1999).
21. E. Wolf, "Three-dimensional structure determination of semi-transparent objects from holographic data," *Opt. Commun.* **1**(4), 153–156 (1969).
22. W. Choi et al., "Tomographic phase microscopy," *Nat. Methods* **4**(9), 717–719 (2007).

23. Y. Sung et al., "Optical diffraction tomography for high resolution live cell imaging," *Opt. Express* **17**(1), 266–277 (2009).
24. Y. Cotte et al., "Marker-free phase nanoscopy," *Nat. Photonics* **7**(2), 113–117 (2013).
25. M. Lee et al., "Isotropically resolved label-free tomographic imaging based on tomographic moulds for optical trapping," *Light Sci. Appl.* **10**(1), 102 (2021).
26. F. Merola et al., "Tomographic flow cytometry by digital holography," *Light Sci. Appl.* **6**(4), e16241 (2017).
27. C. Zuo et al., "Wide-field high-resolution 3D microscopy with Fourier ptychographic diffraction tomography," *Opt. Lasers Eng.* **128**, 106003 (2020).
28. R. Ling et al., "High-throughput intensity diffraction tomography with a computational microscope," *Biomed. Opt. Express* **9**(5), 2130–2141 (2018).
29. Y. Baek and Y. Park, "Intensity-based holographic imaging via space-domain Kramers–Kronig relations," *Nat. Photonics* **15**(5), 354–360 (2021).
30. M. Chen et al., "Multi-layer Born multiple-scattering model for 3D phase microscopy," *Optica* **7**(5), 394–403 (2020).
31. J. Li et al., "Transport of intensity diffraction tomography with non-interferometric synthetic aperture for three-dimensional label-free microscopy," *Light Sci. Appl.* **11**(1), 154 (2022).
32. L. Tian and L. Waller, "3D intensity and phase imaging from light field measurements in an LED array microscope," *Optica* **2**(2), 104–111 (2015).
33. L. Tian et al., "Computational illumination for high-speed *in vitro* Fourier ptychographic microscopy," *Optica* **2**(10), 904–911 (2015).
34. L. Tian et al., "Multiplexed coded illumination for Fourier ptychography with an LED array microscope," *Biomed. Opt. Express* **5**(7), 2376–2389 (2014).
35. Y. Fan et al., "Optimal illumination scheme for isotropic quantitative differential phase contrast microscopy," *Photonics Res.* **7**(8), 890–904 (2019).
36. N. Streibl, "Three-dimensional imaging by a microscope," *J. Opt. Soc. Am. A* **2**(2), 121–127 (1985).
37. J. M. Soto, J. A. Rodrigo, and T. Alieva, "Label-free quantitative 3D tomographic imaging for partially coherent light microscopy," *Opt. Express* **25**(14), 15699–15712 (2017).
38. G. Kim et al., "Holotomography," *Nat. Rev. Methods Primers* **4**(1), 51 (2024).
39. S. Zhou et al., "Transport-of-intensity Fourier ptychographic diffraction tomography: defying the matched illumination condition," *Optica* **9**(12), 1362–1373 (2022).
40. J. Hong et al., "High-speed holotomography of live cells and tissues using multi-pattern sparse axial scanning," *Opt. Express* **33**(22), 45708–45720 (2025).
41. J. Sun et al., "High-speed Fourier ptychographic microscopy based on programmable annular illuminations," *Sci. Rep.* **8**(1), 7669 (2018).
42. P. Thibault et al., "Probe retrieval in ptychographic coherent diffractive imaging," *Ultramicroscopy* **109**(4), 338–343 (2009).
43. Y. Gao and L. Cao, "Motion-resolved, reference-free holographic imaging via spatiotemporally regularized inversion," *Optica* **11**(1), 32–41 (2024).
44. C. Zuo et al., "Transport of intensity equation: a tutorial," *Opt. Lasers Eng.* **135**, 106187 (2020).
45. S. Zhou et al., "Accelerated Fourier ptychographic diffraction tomography with sparse annular LED illuminations," *J. Biophotonics* **15**(3), e202100272 (2022).
46. J. Lim et al., "Comparative study of iterative reconstruction algorithms for missing cone problems in optical diffraction tomography," *Opt. Express* **23**(13), 16933–16948 (2015).
47. J. Li et al., "High-speed *in vitro* intensity diffraction tomography," *Adv. Photonics* **1**(6), 066004 (2019).
48. R. Wang et al., "Video-rate gigapixel ptychography via space-time neural field representations," arXiv:2511.06126 (2025).
49. A. Saba et al., "Physics-informed neural networks for diffraction tomography," *Adv. Photonics* **4**(6), 066001 (2022).
50. L. Lu et al., "Physics-informed deep learning transport-of-intensity quantitative phase imaging: accurate phase retrieval under partially coherent illumination," *Intell. Opto-Electron.* **1**(2), 250005 (2025).
51. D. Dong et al., "Super-resolution fluorescence-assisted diffraction computational tomography reveals the three-dimensional landscape of the cellular organelle interactome," *Light Sci. Appl.* **9**(1), 11 (2020).
52. Z. Chen and M. Segev, "Highlighting photonics: looking into the next decade," *eLight* **1**(1), 2 (2021).
53. S. Song et al., "Polarization-sensitive intensity diffraction tomography," *Light Sci. Appl.* **12**(1), 124 (2023).
54. S. Shin et al., "Tomographic measurement of dielectric tensors at optical frequency," *Nat. Mater.* **21**(3), 317–324 (2022).
55. A. C. Kak and M. Slaney, *Principles of Computerized Tomographic Imaging*, SIAM (2001).
56. C. McCutchen, "Generalized aperture and the three-dimensional diffraction image," *J. Opt. Soc. Am. A* **54**(2), 240–244 (1964).
57. B. Chen and J. J. Stamnes, "Validity of diffraction tomography based on the first Born and the first Rytov approximations," *Appl. Opt.* **37**(14), 2996–3006 (1998).
58. A. Devaney, "Inverse-scattering theory within the Rytov approximation," *Opt. Lett.* **6**(8), 374–376 (1981).
59. D. P. Bertsekas, "Incremental proximal methods for large scale convex optimization," *Math. Program.* **129**(2), 163–195 (2011).

Shun Zhou received his BE degree from Nanjing University of Science and Technology (NJUST). He is a fourth-year PhD student in optical engineering at NJUST. His research interests include computational optical imaging, phase retrieval, and intensity diffraction tomography. He is a member of SPIE and Optica.

Qian Shen is a PhD student in optical engineering at Naniing University of Science and Technology. Her research interests include quantitative phase imaging and computational imaging. She is a member of SPIE and Optica.

Habib Ullah is pursuing his PhD degree at the School of Electronic and Optical Engineering, Nanjing University of Science and Technology. His research interests include diffraction tomography microscopy, refractive index reconstruction, and computational imaging.

Kaiyu Du received his BE degree from Wuhan Institute of Technology and is currently pursuing his ME degree at Nanjing University of Science and Technology. His research interests include computational microscopy and diffraction tomography.

Linpeng Lu received her BE degree and PhD in optical engineering from Nanjing University of Science and Technology (NJUST) in 2018 and 2024, respectively. She is currently a postdoctoral researcher at the School of Electronic and Optical Engineering, NJUST. Her research interests focus on computational microscopy imaging. She is the principal investigator of a National Natural Science Foundation of China (NSFC) Youth Program and is a member of SPIE and Optica.

Hongjun Wu received her MS degree from Tiangong University in 2019 and PhD from Peking Union Medical College & Tsinghua University in 2022. She has been a lecturer at Nanjing University of Science and Technology since 2022, specializing in the principle and application of fluorescence super-resolution microscopy technology.

Yao Fan received her BS degree and PhD from Nanjing University of Science and Technology (NJUST) in 2015 and 2022, respectively. She is currently an associate professor in the Department of Optoelectronic Technology at NJUST. Her research interests include computational

optical imaging, digital holography, phase retrieval, and quantitative phase imaging. She is a member of SPIE and Optica.

Jiasong Sun received his BS degree from Soochow University in 2012 and his PhD from Nanjing University of Science and Technology (NJUST) in 2019. He is currently an associate professor and is conducting research at the Smart Computational Imaging Laboratory at NJUST, focusing on computational microscopic imaging, quantitative phase imaging, and super-resolution microscopy. He has published more than a dozen papers in journals including *PhotoniX*, *Laser & Photonics Reviews*, *Optica*, and *ACS Photonics*. His work has received over 5000 citations on Google Scholar.

Dayong Jin received his PhD from Macquarie University, Australia, in 2007. He is a distinguished professor at the University of Technology Sydney and a Chair Professor at the Eastern Institute of Technology. He is an ARC Laureate Fellow, a Fellow of the Australian Academy of Technology and Engineering, and a Fellow of the American Institute for Medical and Biological Engineering. He has been recognised as a Clarivate Top 0.1% Highly Cited Researcher since 2021. His expertise spans biomedical engineering, nanotechnology, microscopy, microfluidics, and analytical chemistry, with a focus on enabling rapid and sensitive detection of cells and biomolecules.

Qian Chen received his BS, MS, and PhD degrees from Nanjing University of Science and Technology. He is currently working as a professor and president at North University of China. He has been selected as Changjiang Scholar Distinguished Professor. With broad research interests in photoelectric imaging and information processing, he has authored more than 200 journal papers. His research team develops novel technologies and systems for non-interferometric quantitative phase imaging and high-speed 3D sensing and imaging with particular applications in national defense, industry, and bio-medicine.

Chao Zuo received his BE degree and PhD from Nanjing University of Science and Technology (NJUST) in 2009 and 2014, respectively. He is a Zijin Chair Professor at NJUST, distinguished professor of "Changjiang Scholars Program". He leads the Smart Computational Imaging Laboratory (SCILab: www.scilaboratory.com) at the School of Electronic and Optical Engineering, NJUST, and is also the founder and director of the Smart Computational Imaging Research Institute of NJUST. He has long been engaged in the development of novel *Computational Optical Imaging and Measurement* technologies, with a focus on *Phase Measuring Imaging Metrology*. He has published >300 peer-reviewed articles with over 20,000 citations. He is a Fellow of SPIE, Optica, and IOP, and listed as a Clarivate Highly Cited Researcher.